Lab-based X-ray imaging for accurate seismic velocity measurements at high pressure

N. Backhouse[1*], A.R. Thomson[1*] (a.r.thomson@ucl.ac.uk), C. Wilson[2], B. Rayner[1], I.G. Wood[1], N. Hughes[1], M. Zahir[1] and J.P. Brodholt[1,3]

[1)]Department of Earth Sciences, University College London, London, UK

[2)]AWE, Reading, Berkshire, UK

[3)]Centre for Planetary Habitability (PHAB), University of Oslo, Oslo, Norway

*joint 1st authors

(Dated: 7th September 2026)

A novel approach for accurately measuring the compressional (P) and shear-wave (S) velocities of materials at high pressure is demonstrated up to ~6 GPa using a Paris-Edinburgh press. Typically, accurate ultrasonic velocity measurements at high pressure require synchrotron facilities to image the sample length *in-situ* and to determine the internal cell pressure using X-ray diffraction from an internal standard. Here, replacing synchrotron-based imaging, sample lengths are directly measured *in-situ* using a custom-built divergent-beam X-ray imaging system in a university laboratory. The imaging system combines a microfocus source, an X-ray fluorescent scintillator, magnification optics and a high-sensitivity CMOS camera to obtain radiographic X-ray images of comparable quality to those obtained at synchrotron facilities in exposures of ~ 10 seconds. We demonstrate the capabilities of the system with *in-situ* velocity measurements of a natural novaculite (quartz) sample throughout compression. Measured velocities are accurate to ± 0.3% on average. In place of a diffraction-based pressure calibrant, we demonstrate that pressures can be determined from the observed velocities of the novaculite sample by using literature elasticity data of quartz. Experimental pressures were shown to extend to 5.8 GPa, with all reported pressure conditions accurate to better than ± 0.3 GPa. Finally, the compressional wave travel time of the alumina buffer rod has been calibrated as a pressure marker for use in future compression experiments.

I. INTRODUCTION

Pulse-echo ultrasonic measurements are widely used for determining a material's elastic properties[1, 2]. As well as geophysically relevant minerals, this approach has been used on nuclear fuel materials[3], gases[4], liquids[5, 6], plastics[7] and biological tissues[8, 9] amongst others.

In the geosciences, acoustic velocity data are required to understand the origin of seismological observations from planetary interiors. The elastic properties of minerals and melts are needed to interpret seismic observations in terms of something physically meaningful; e.g. variations in temperature, mineralogy and bulk chemistry. Whilst the strategy of interpreting seismic velocity profiles using experimental elasticity data has been used in studies for over 70 years[10], this approach remains problematic as experimentally obtained elastic data on minerals and melts are extremely sparse at mantle pressure (P) and temperature (T) conditions.

In lieu of data, seismological interpretations widely use software packages[11-13] based upon thermodynamic datasets of mantle materials[14-18]. Whilst such software and datasets provide an invaluable tool and are calibrated using available data, many minerals and most melt compositions have never had their velocities measured at appropriate PT conditions. Arguably improving the underlying dataset of mineral and melt elastic properties is probably the most meaningful route towards improving our understanding of planetary interiors, but collecting velocity data at high pressure is not trivial.

Recovering accurate elasticity data in any ultrasonic experiments requires two separate measurements; the ultrasonic travel time (Δt) and the sample length (l). These combine such that the measured velocity (compressional or shear wave) is obtained from $v = 2l/\Delta t$. In high pressure experiments direct access for length measurements is limited by opaque hydraulic, confining and pressure-generating components. If the sample behaved totally elastically during compression, then one could estimate the sample length using the original length, the sample pressure and an a equation of state[19]; however sample deformation is rarely truly elastic (especially during initial compression) possibly explaining why lab measurements often diverge from *in-situ* data[20, 21]. This strongly implies reliable and accurate measurements require synchrotron-like capabilities for sample imaging. A secondary benefit of using synchrotron X-rays is they simultaneously allow quantification of sample pressure via diffraction from a pressure standard[2]. However, the need for synchrotron access severely limits the number of studies that can be achieved as there are only a few suitable facilities, with beamtime being competitively awarded.

Here we describe a novel, lab-based, X-ray imaging system allowing *in-situ* radiographic imaging comparable to that achieved at a synchrotron facility. This can be utilised in ultrasonic experiments to accurately determine sample length, and therefore

velocity, at high pressure. We demonstrate this approach with measurements of a polycrystalline quartz sample throughout compression in a toroidal Paris-Edinburgh (PE) assembly.

II.THE X-RAY IMAGING SYSTEM

The X-ray imaging system described is heavily inspired by the approach used at synchrotron large volume press beamlines[22-26]. Absorption X-ray radiographs of high-pressure samples are collected by means of a phosphorescent scintillator placed behind the sample in the x-ray beam. The light emitted is subsequently optically magnified and imaged using a low-noise camera. The main differences between this setup and a synchrotron beamline are the divergent beam and significantly lower X-ray flux of the lab X-ray source. Ultimately, this means that additional optimisation of the scintillator efficiency and camera system is required to achieve radiographs with suitable signal-to-noise statistics.

Currently our lab-based imaging system uses a W-filament microfocus X-ray source (Hamamatsu L9421-02), mounted on a manual lab-jack such that its height can be easily matched to the sample position. The source operates at an excitation voltage of 40-90 kV, producing a Bremsstrahlung X-ray spectrum in a beam having a focal spot size of 5-7 µm and a cone angle of 39°.

The sample environment in this study is a V3B PE press equipped with customised toroidal anvils. During measurements the press is mounted horizontally on a custom-made stand that allows small rotations of the press around a vertical axis to correct for any small tilts that may occur in the sample during initial loading. The stand is additionally designed to allow a safe, and relatively straightforward, transfer of the press in/out of the X-ray enclosure. To compensate for the motion of the sample assembly caused by ram advance during compression, the entire press is mounted on a linear stage (ISEL LES-5) with integrated MS200HT2 stepper motor. Finally, the stand also incorporates a rotational stepper motor allowing full 360° rotation of the PE-press to allow collection of datasets suitable for tomographic reconstructions in future studies.

Downstream from the sample environment, X-ray projections are converted into optical images for capture using an X-ray microscope system equipped with GAGG(Ce) scintillator (Ce-doped Gadolinium Aluminium Gallium Garnet) and a 4X optical objective lens from Optique Peter. Optical images pass via an enclosed path and are recorded using a low-noise scientific camera (currently either a Hamamatsu ORCA Fusion CMOS or QSI 660 CCD). This entire imaging system is mounted on optical rails allowing its height to be adjusted to match the source and sample height. The effective pixel size on the scintillator using this setup is either 1.6 or 1.1 µm depending on whether the Hamamatsu or QSI camera is in use. Due to the divergent nature of the X-ray beam, the true pixel size of any real sample image will be smaller than this, depending on the source-sample-detector geometry. As the system geometry is variable, a pixel size calibration is required as the first step of every experiment. The complete imaging system is mounted on an optical table and housed in a Pb-lined X-ray enclosure as shown in the system schematic (Figure 1).

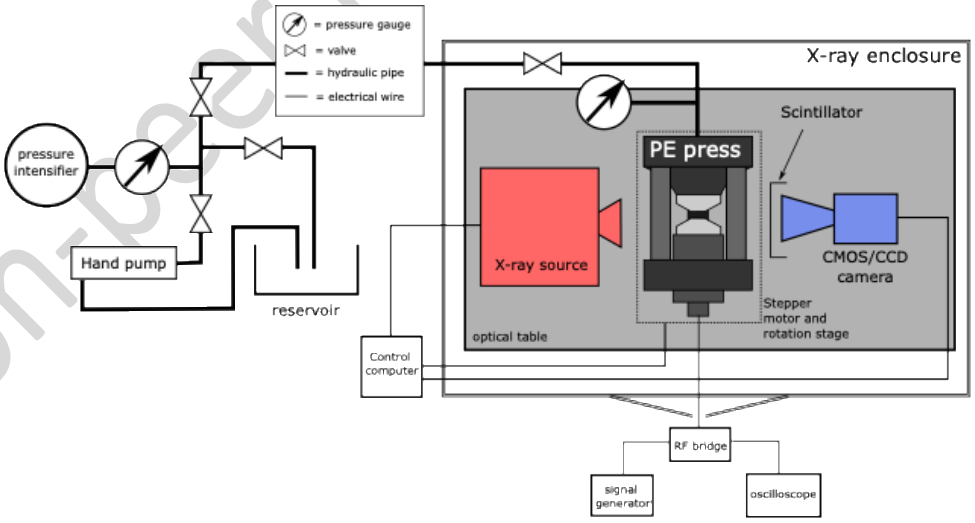

Figure 1: *Schematic diagram (not to scale) of the lab-based X-ray imaging system. The X-ray source, sample stage with PE press and CMOS/CCD camera (shown here as viewed from above) are all mounted on an optical table inside the interlocked X-ray enclosure. The control computer and hydraulic pressurisation system are positioned outside the enclosure with access through a labyrinth at one end behind the X-ray source. Ultrasonic waves are generated and received by a $LiNbO_3$ transducer mounted on the rear of the upper anvil through access in the breach, where connections are made to RF equipment.*

III.EXPERIMENTAL METHODS and DATA

Sample

A natural novaculite (fine-grained polycrystalline quartz) from UCL's rock collections was used throughout this study. X-ray powder diffraction patterns of a polished slice of the bulk sample were collected using a lab diffractometer and at ID06-LVP of the ESRF. At UCL a Panalytical X'Pert Pro diffractometer operating with Fe-filtered Co Kα radiation (40 kV / 30 mA) was used in Bragg-Brentano geometry, effectively making a surface measurement of an area sized ~ 10 x 10 mm. In contrast, diffraction at the ESRF was collected from a 0.5 x 0.5 mm area using a monochromatic beam (λ = 0.23393Å) in forward-scattering transmission geometry through the ~ 2.6mm sample slice. Rietveld refinements of show the starting material to consist of between 98.8 vol.% (ESRF data) and 99.4 vol.% (UCL data) quartz, with trace calcite and dolomite (see Supplementary Figure 1). Visual inspection of the sample suggests the carbonate is likely to be heterogeneously distributed throughout the sample and, as such, cylindrical samples with diameter 1.5 mm were cut from apparently homogenous regions where carbonate content was believed to be minimal. Samples were ground to the desired initial lengths and their faces polished to a finish using 1μm diamond paper. The velocities, both v_P and v_S, of the polished slice characterised by X-ray diffraction, whose thickness was measured using digital callipers as 2.579(2) mm, were determined using the same ultrasonic methods described below (Supplementary Table 1).

Toroidal PE press assembly

Experimental assemblies consisted of a toroidal gasket that was compressed between opposing anvils with central depressions housing the sample setup. In relatively recent studies PE assemblies have generally used anvils containing a central conical depression with a flat base and diameter close to 3mm [25, 27, 28]. Whilst this geometry can generate conditions up to ~ 7 GPa [29], it experiences a rapidly closing anvil gap with increasing pressure. For ultrasonic studies where it is essential to image the entire sample for accurate sample length measurements this is a major limitation.

To reduce the anvil gap closure and improve pressure efficiency, we have adopted modified Drickamer-style anvils and assemblies, similar to those described by [30-32]. The main modification from the previous designs is the use of a flat-bottomed anvil depression to house a buffer rod for efficient ultrasonic wave propagation (Supplementary Figure 2). Experience from trial experiments demonstrates that this assembly-anvil geometry maintains anvil gaps of > 1mm to the maximum load tested to date (~ 800 bar in a different test experiment, which is equivalent to > 6 GPa based on this study).

Assemblies (Figure 2) consist of 4:1 boron epoxy gaskets, pressed to have a profile matching the anvils, housed within a Polyetheretherketone (PEEK) confining ring. ZrO_2 caps provide efficient pressure generation alongside thermal insulation for future high temperature studies. Inner parts consist of hBN, which is sufficiently soft to accommodate the required deformation during initial compression, and MgO.

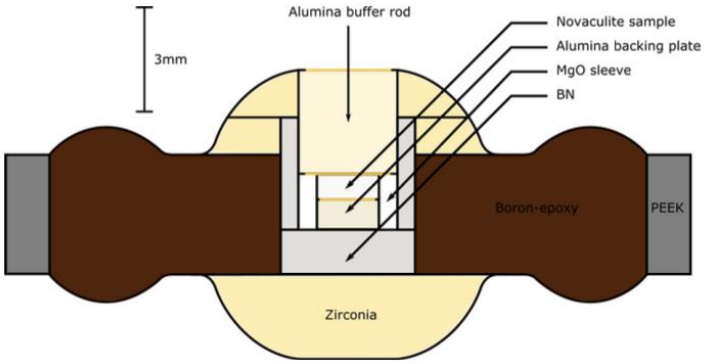

Figure 2: *Scale cross section diagram of the PE press assembly used in the current study. Ultrasonic signals are delivered to/from the novaculite sample via a Al_2O_3 buffer rod, with each component separated by 2 µm Au foils. The boron epoxy gasket is manufactured using a custom mould to form a toroidal profile to match the anvils.*

Within assemblies, the ultrasonic column consists of a 2 mm diameter Al_2O_3 buffer rod, sample and Al_2O_3 backing plate stack backed by hBN. The buffer rod length (2.608(1) mm in this experiment) was chosen to ensure the top of the sample can be clearly identified next to the upper anvil. In the experiment reported here, the sample length was measured to be 715 ± 1 µm prior to loading**.** The sample and backing plate are contained within a machined MgO sleeve (2.0 mm outer, 1.5 mm inner diameter). The incorporation of the alumina backing plate was found to alleviate the most significant deformation and rotation

of the sample during initial compression. Repeated experiments also revealed that thin backing plates are more prone to cracking during compression and in the reported run a 1mm length alumina plate was used. Each component in the ultrasonic column was separated using 2 µm thick Au foils which act both as radiographic positional markers and aids for acoustic coupling.

Pressure was applied to the sample via a screwjack-style pressure intensifier, capable of maximum oil pressures of ~ 1550 bar. After initial anvil closure, the PE press was rotated around the sample position until the dark bands caused by the gold foil were observed to be their thinnest and darkest. This "sharpening" of the image indicates that the sample is perpendicular to the x-ray beam path effectively compensating for small internal tilts within the assembly introduced during loading. An initial radiograph, coupled with the known initial sample length measured using digital calipers, was used to calibrate the pixel size of the images throughout this study.

Ultrasonic measurements

Ultrasonic signals, each consisting of a single frequency burst of 3 sine waves, were generated by a Keysight 33600A series waveform generator and passed using a Keysight 86205A RF bridge to a dual mode 10° rotated Y-cut $LiNbO_3$ transducer. This transducer simultaneously produces both P and S waves, but the relative intensity of these ultrasonic components varies with frequency. The transducer itself was fixed to the rear side of the upper PE press anvil using EpoTek 353ND epoxy. Returning echoes from within the sample assembly were collected using the same transducer and passed via the RF bridge to a Keysight DSOS104A digital oscilloscope. Ultrasonic traces from 16-60 MHz (at 2 MHz intervals) were collected at 10 bar increments.

X-ray radiographs of the sample, allowing accurate sample length measurements, were also collected at matching 10 bar increments. Individual radiographs used exposure times of 10 seconds, with X-ray conditions of 90 kV and 89µA (Figure 3). For this application raw radiographs, without dark and/or flat field corrections, were sufficient to allow sample lengths to be extracted using the TravelDistance module within the SonicPy GUI[33]. This software allows polynomials to be plotted through the intensity minima within regions of interest corresponding to the centre of each Au marker foil. Sample lengths are subsequently determined as the average distance between polynomial functions representing the foils at either end of the sample. As intensity minima were fitted as Gaussian absorption functions, length uncertainties were estimated as double the Gaussian function width[34].

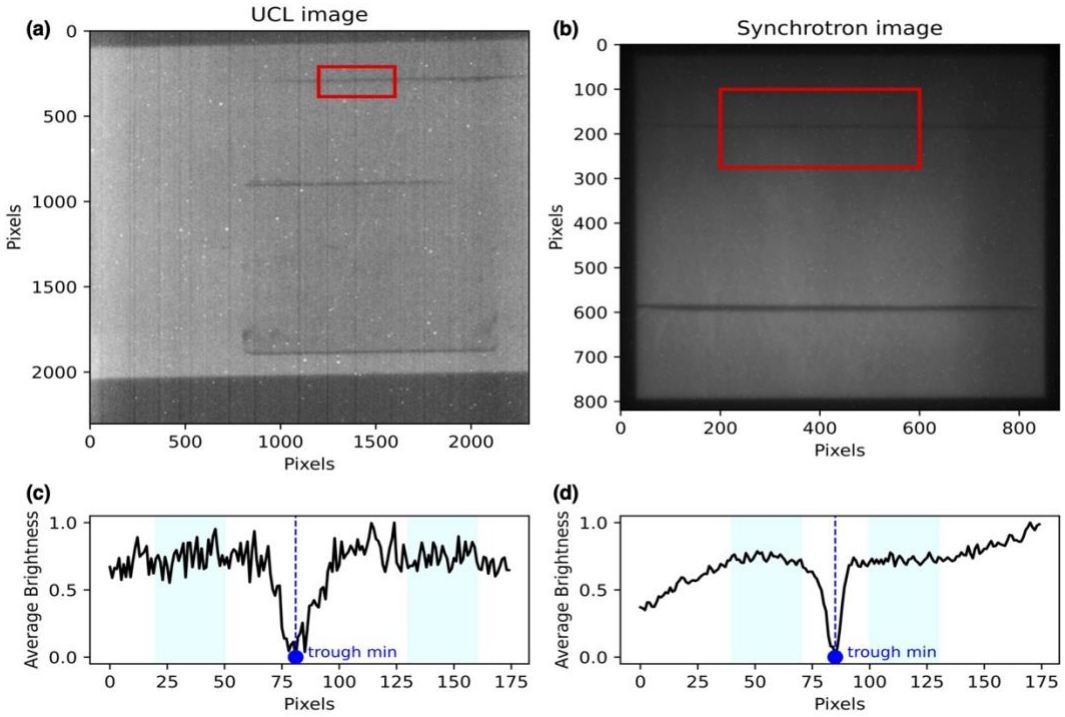

Figure 3: ***(a)*** *representative 10 second X-ray radiograph of the experiment described in this study.* ***(b)*** *representative X-ray radiograph of a synchrotron based PE-press ultrasonic experiment collected at 16-BM-B, HPCAT, APS (Backhouse et al., 2026).* ***(c)*** *and* ***(d)*** *X-ray intensity profiles in a direction perpendicular to the Au marker foil within the red regions of interest indicated in (a) and (b) respectively.*

Figure 3 additionally demonstrates the quality of X-ray radiographs using the UCL imaging system compared with a typical ultrasonic radiographic image collected from a PE press experiment at a synchrotron beamline, in this case instrument 16-BM-B of the Advanced Photon Source (APS), Argonne National Lab (data are from Backhouse et al., in press). This comparison, which is achieved within equivalent regions of interest along profiles extracted perpendicular to the foil, shows that despite higher signal-to-noise ratios (SNR) of synchrotron images (SNR = 4.78), lab data is still perfectly adequate (SNR = 3.16) to identify sample length. Whilst the difference in noise is, in part, due to the imperfections on the scintillator in this lab-based system (visible in the X-ray image as white points) it is predominantly due to the synchrotron image simply being brighter due to orders of magnitude higher X-ray flux.

However, an additional benefit of the lab system relative to synchrotron imaging results from a combination of its divergent nature and optical magnification. Cumulatively, for this application, it means that lab-based radiographic images can have a higher spatial resolution than synchrotron radiographs. In this comparison lab data (Figure 3a) have a pixel edge length of 1.129 µm, whilst APS images (Figure 3b) have an equivalent length of 1.714 µm. In both cases the uncertainty of the length measurements is dominated by non-parallel sample faces/foils, meaning the penumbra effect from the divergent beam can be ignored. This means that the images in Fig. 3 correspond to sample length measurements of 682.3 +/- 0.79 µm (0.12% length uncertainty) at UCL and 696.1 +/- 3.8 µm (0.55% length uncertainty) at the APS, where both length measurements were extracted using the SonicPy GUI. Thus, the quality of the images from the PE press at UCL, while lower than those collected at a synchrotron in statistical terms, are more than sufficient to derive high-quality ultrasonic velocity measurements.

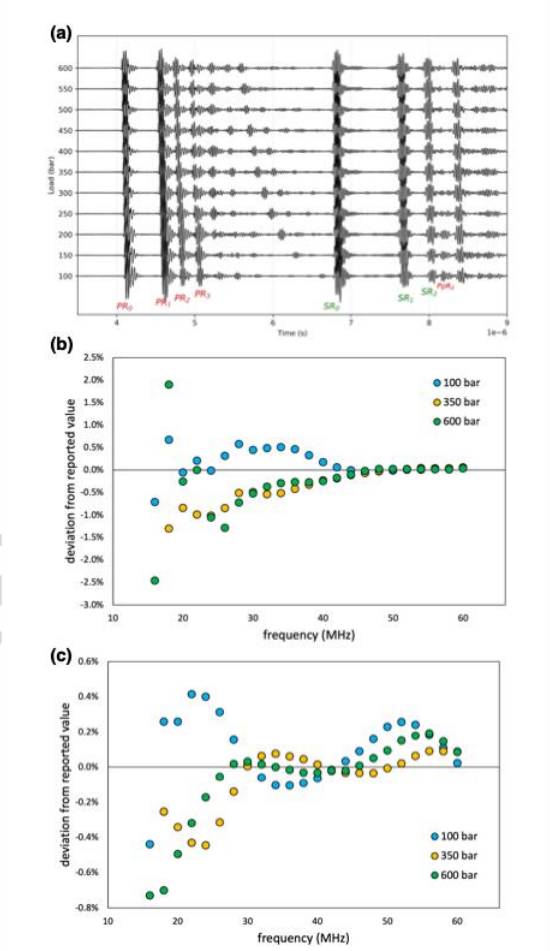

Figure 4: (a) *Stack of representative unprocessed ultrasonic traces from 50 bar intervals from 100 to 600 bar oil pressure in the current study, offset by increasing load on the y-axis. Relevant ultrasonic arrivals are each labelled as xRi; where x indicates whether it is a P- or S-wave arrival, and i indicates which interface the echo is returning from (0 = anvil – buffer rod, 1 = buffer rod – sample, 2 = sample – backing plate, 3 = backing plate – BN).* ***(b)*** *and* ***(c)*** *Plots of frequency-corrected P-wave and S-wave travel time in the novaculite sample as a function of frequency for a representative dataset collected at xx bars. Reported travel times are the mean of all measurements between 40-60 MHz for P-waves and 20-40 MHz for S-waves.*

IV. RESULTS

No returning ultrasonic echoes were observed until over 100 bar oil pressure was reached in this experiment. Initial compression is assumed to reflect the closing of free space inside the assembly, initial gasket flow and associated crack/grain boundary closure in the sample. Thus, the first ultrasonic spectrum recorded is presumed to represent the crack-free sample velocity at zero pressure and is taken as t_P^0 and t_S^0. This interpretation is confirmed as velocities calculated at these conditions fall within 2σ uncertainty of ambient starting material measurements (Supplementary Table 1).

From this point onwards ultrasonic travel times at each load were determined via cross-correlation of the returning echoes from the top and bottom of the sample (e.g R1 and R2 in Figure 4a), i.e. by using the pulse-echo overlap method[35]. Raw travel time measurements were corrected to account for the effect of the gold foils in the acoustic path[36]. Fitted P and S wave travel times were observed to be constant over a range of frequencies, such that P-wave values used throughout the remainder of this study's text are the mean of all corrected data from 44-60 MHz (figure 4b) and S-wave travel times are the mean of corrected 28-48MHz data (Fig. 4c). Reported uncertainties reflect the standard error in the mean of these measurements. Data are reported in Supplementary Table 1.

The evolution of radiographs and derived sample length measurements with uncertainties are plotted in Figure 5a. This shows that the sample shortened ~ 10% by 610 bar load with the rate of shortening decreasing as expected throughout hydrostatic compression. Figure 5c demonstrates there was no degradation of radiograph quality with increasing load, nor is any unwanted sample deformation or tilting observed. Additionally, since the field of view is constant in all radiographic images (~2.08 mm), the closure of the anvil gap is also observed, with a gap of > 1.3 mm maintained at 610 bars.

Velocities of the novaculite (quartz) sample at each pressure were determined from travel time (Δt) and length (l) measurements, $v = 2l/\Delta t$. Errors in reported velocities are fully propagated from uncertainties in both measurements as

$$\Delta v = v\sqrt{\left(\frac{\Delta l}{l}\right)^2 + \left(\frac{\Delta t}{t}\right)^2} \qquad \text{(eq 1)}$$

The evolution of sample velocity with increasing oil pressure is plotted in Fig 5b. Compressional and shear velocities were observed to vary smoothly from 6.03(2) and 3.92(1) km.s^{-1} at 100 bar to 6.66(1) and 3.80(1) km.s^{-1} at 610 bar. v_P/v_S measurements of the sample, which can be derived directly from ultrasonic travel times without the requirement for length measurements (calculated as t_S/t_P), are observed to increase from 1.549(3) to 1.751(3) between 100 and 610 bars oil pressure. These data demonstrate that measurements of v_P, v_S and v_P/v_S have mean accuracies of 0.31, 0.32 and 0.20% respectively up to 610 bars load in this experimental configuration.

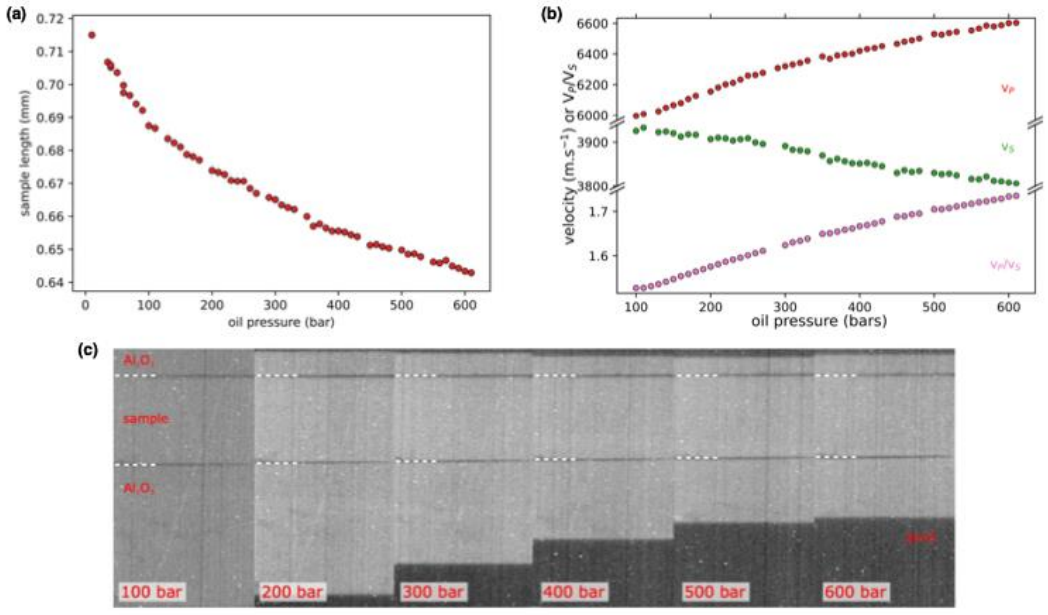

Figure 5: (a) *Plot of measured sample length with standard error (in mm) as a function of oil pressure.* ***(b)*** *Derived v_P, v_S and v_P/v_S of the novaculite samples as a function of oil pressure.* ***(c)*** *10 second X-ray radiographs at 100 bar increments*

demonstrating the evolution of sample length throughout the experiment. Dark regions at the top and bottom of the images are anvils, and the sample sits between the two Au (dark) marker foils.

V. DISCUSSION

One obvious consequence of performing ultrasonic experiments away from a synchrotron beamline is the lack of X-ray diffraction data, meaning pressure cannot be determined from measurements of a pressure marker's unit-cell volume. However, it has previously been shown that ultrasonic travel times/velocities of materials with known elasticity at high pressure can be used as alternative "off-line" pressure calibrants [37-39]. Here we utilise literature data to use the polycrystalline quartz sample to act as a pressure marker in this study, facilitating calibration of the buffer rod travel time for use in further experiments following the approach of Wang *et al.* [39].

Elastic properties of quartz

Whilst the physical properties of quartz have been studied many times, the analyses presented here use the elasticity data from single crystal Brillouin spectroscopy reported recently [40]. This study utilised an optical grade quartz single crystal, compressed in a medium of methanol:ethanol:water (16:3:1) ensuring hydrostatic conditions were maintained to 10 GPa [41], with pressure monitored using ruby fluorescence [42]. We adopt the assumption from [40] that pressure follows a third-order Birch-Murnaghan equation of state:

$$P = \frac{3}{2}K_{0T}\left[\left(\frac{V_0}{V}\right)^{\frac{7}{3}} - \left(\frac{V_0}{V}\right)^{\frac{5}{3}}\right]\left\{1 + \left(\frac{3}{4}\right)(K'_{0T} - 4)\left[\left(\frac{V_0}{V}\right)^{\frac{2}{3}} - 1\right]\right\} \quad \text{(eq 2)}$$

where K_{0T} = 37.4 (6) GPa and K_{0T}' = 6.2 (2). Subsequently, to ensure c_{ij} measurement uncertainties from Wang et al. (2015) are fully propagated to our pressure estimates the pressure evolution of all six independent elastic constants were refitted using the same third-order finite-strain equations as previously employed [40]:

$$c_{ijkl}(f) = (1 + 2f)^{\frac{7}{2}}\left[c^0_{ijkl} + b_1 f\right] - P\Delta_{ijkl} \quad \text{(eq 3)}$$

$$b_1 = 3K_0\left(c'_{ijkl} + \Delta_{ijkl}\right) - 7c^0_{ijkl} \quad \text{(eq 4)}$$

$$\Delta_{ijkl} = -\delta_{ij}\delta_{kl} - \delta_{ik}\delta_{jl} - \delta_{il}\delta_{jk} \quad \text{(eq 5)}$$

where $f = \left(\frac{1}{2}\right)\left[(V_0/V)^{2/3} - 1\right]$, c^0_{ijkl} and c'_{ijkl} are the ambient pressure constants and their pressure derivatives and δ_{ij} is the Kronecker delta. Whilst we initially adopted the reported measurement uncertainties in each elastic constant as absolute weightings during linear regression, inspection of results revealed far more than 4.55% of data fall outside the 2-sigma confidence limits implying the true uncertainties are larger than reported (blue confidence intervals in Supplementary Figure 3). Thus, in attempt to ensure the reported uncertainties in pressures are not underestimated, elastic constants were refitted assuming reported measurement errors only reflect their relative uncertainties (red confidence intervals in Supplementary Figure 3). Fitted elastic constants were used to evaluate the Voigt bound, Reuss bound and Voigt-Reuss-Hill (VRH) average velocities (and their uncertainties) for polycrystalline quartz at ambient temperature and increasing pressure (Supplementary Figure 4).

Pressure estimation from quartz velocities

Assuming the 100 bar data is representative of zero pressure, comparison of modelled compressional and shear wave velocities with measurements from this study show that experimental v_P and v_S are both lower than estimates using the absolute value of the VRH averaging scheme. Whilst the experimental v_P only deviates slightly from the literature ambient pressure measurement [40], the measured v_S is significantly lower than the model VRH value at ambient conditions. However, since both (i) match ambient measurements within uncertainty, (ii) fall within uncertainties of the Voigt and Reuss bounds and (iii) recent similar ultrasonic measurements of novaculite observed a similar v_P but an even lower initial shear wave velocity at ambient conditions (namely 3.89 km.s^{-1})[43], it is clear we are measuring the correct velocities and the properties of novaculite are not exactly the same as synthetic single-crystal quartz. No-matter the cause of this offset, it is observed that modelled Voigt, Reuss and VRH velocities of quartz have sub-parallel pressure dependences to at least 6 GPa pressure. Thus, to simplify analyses, model properties are compared with normalised velocity measurements when estimating pressures (similar to [38, 39]).

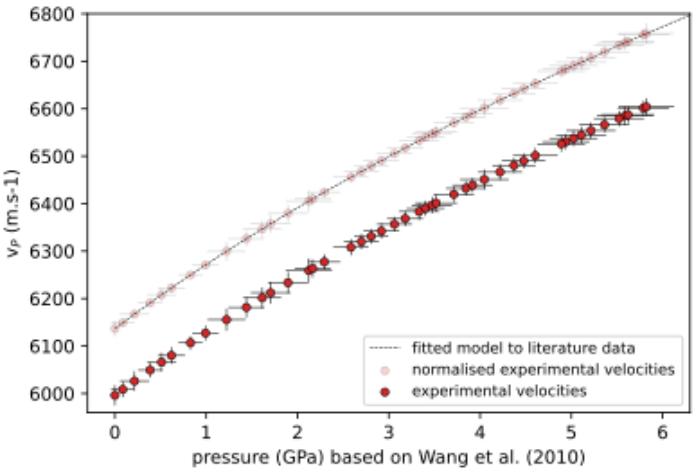

Figure 6: *Estimated pressure with uncertainties, derived from fitting the P-wave travel time to equations based on Wang et al. (2015) as described in the text, vs measured sample v_P (solid symbols). The dashed line shows fitted model values of quartz's v_P^{VRH} with pressure, and pressure in this experiment is estimated using normalised P-wave velocities (transparent symbols).*

Based upon a simplification of finite strain theory [44], we assume that, at least over the modest pressures achievable using the PE-press, the pressure dependence of velocities in quartz are adequately described by:

$$v_P = v_P^0 \times (1 + Af) \qquad \text{(eq 6)}$$

where v_P^0 is the ambient pressure velocity (which is fitted), f is strain as above, and A is a fitted parameter. Fitting model v_P data for quartz this approach yields v_P^0 = 6137(9) m s^{-1} and A = 2.65(5) (Supplementary Figure 5). This can be applied to estimate experimental pressure from polycrystalline quartz velocities by normalising velocity measurements to v_P^0 and using the third order Birch-Murnaghan equation of state parameters via eq 2. Estimating experimental pressures from ultrasonic measurements in this way gives sample conditions of ~ 5.8(4) GPa at 610 bar. Throughout the entire experiment uncertainties in pressure estimates using the compressional wave velocity of polycrystalline quartz vary from ±0.13 GPa near ambient to ± 0.37 GPa at 5.8 GPa (Figure 6). This is very comparable to uncertainties achieved using X-ray diffraction-based pressure standards at synchrotron beamlines, demonstrating the possibility of recovering accurate material velocity measurements at known pressures without requiring synchrotron access. In this case, the limit on reducing these uncertainties is the underlying data describing the elastic properties of quartz .

Alumina buffer rod travel time as a pressure marker

Whilst the inclusion of an ultrasonic pressure marker in every experiment is technically possible, a more practical solution exploits the presence of the buffer rod that is required for delivery/receipt of ultrasonic signals. Based on the arguments discussed by Wang et al. [39], the normalised travel time in the Al_2O_3 buffer rod, once calibrated, provides an *in-situ* pressure marker that naturally accounts for the compressional environment of that cell assembly. Observing that the reduction in t_P of the buffer rod is greater than observed for t_S, it is apparent that a pressure calibration based on compressional waves can be more sensitive. Figure 7a shows the normalised travel time t_P/t_P^0 follows an approximately linear dependence described by:

$$P(GPa) = 172.7(30) \times (0.9969(4) - t_P/t_P^0) \qquad \text{(eq 7)}$$

Provided only minimal changes are made to the initial buffer rod length, this provides a useful pressure calibration for repeated experiments using the same PE-press setup. The uncertainty associated with this linear fit is evaluated using the standard error, $\sigma_P = \sqrt{\frac{\sum_{i=1}^{n}(\Delta P_i)^2}{n-1}}$, where ΔP_i is the difference in the calculated pressure via equations 6 and 7 and n is the number of data points. Using all 45 available data the standard error in pressure predictions using the Al_2O_3 buffer rod travel time (compared to estimates from the sample velocity directly) is ± 0.14 GPa. This is comparable with the pressure uncertainty derived from the SiO_2 sample, and is somewhat smaller than that reported for previous ultrasonic buffer rod pressure calibrations (± 0.18 GPa [39]). However, we note that this estimate of pressure uncertainty is only related to the comparison of the two pressure estimates in this study and does not explicitly account for uncertainty in the properties of pressure calibrant, which is quartz in this case.

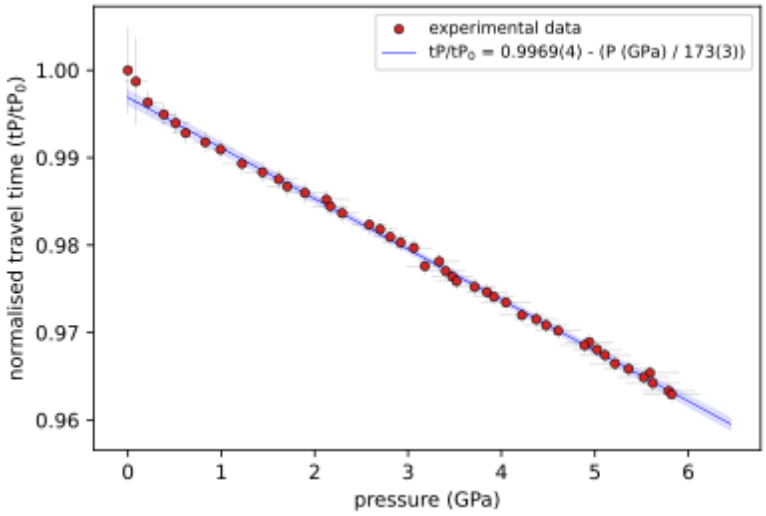

Figure 7: *Normalised P-wave travel time of the alumina buffer rod as a function of pressure calculated using the elasticity of quartz as described in the text. Symbols, and uncertainties, plot experimental measurements, with the blue line showing the linear least squares regression with 2-sigma confidence limits.*

Comments on quartz as a pressure calibrant

Whilst the discussion above demonstrates the capability for accurate lab-based velocity measurements and pressure quantification, it is apparent that polycrystalline quartz is not the ideal calibration material. As a naturally fine-grained material with simple chemistry and many literature studies of its properties it was a convenient choice. However, being a trigonal material with six independent elastic constants, relatively limited literature data and high-pressure stability (such that it could not be used as a high *PT* calibrant beyond ~2 GPa for example) as well as its potential for large seismic anisotropy, in retrospect it was not the optimum pressure calibrant. The potential for difficulty is somewhat demonstrated in the wide variation in the calculated Voigt and Reuss bounds for v_P and v_S and the observed offset between modelled and measured shear wave velocity even at ambient conditions. Despite these issues, given the evolution of observed velocities in this study followed those expected with increasing pressure, we do not believe that cracks, porosity or changing texture are major contributing factors. However, deployment of an improved pressure calibrant that is more acoustically isotropic with a far smaller deviation between its elastic Voigt and Reuss bounds whilst remaining well-characterised by literature studies would clearly reduce uncertainty in pressure estimates for future studies. Additionally, knowledge of the calibrants high temperature elasticity would allow calibration to be extended to high *PT*, which will ultimately be required to constrain velocities at conditions relevant for planetary interiors. The most obvious options for alternative calibration materials are olivine or periclase, where sufficient high quality high *PT* data likely exists in the published literature, e.g. [45].

V. CONCLUSION

Utilising a custom-built X-ray imaging system combined with MHz ultrasonic interferometry a fully lab-based method for accurate measurements of materials velocities up to ~6 GPa is demonstrated at ambient temperature. Pressures were generated in an opposed toroidal-anvil Paris-Edinburgh press setup where anvil gaps of > 1.3mm were maintained to maximum load tested. *In-situ* X-ray radiographs obtained using a divergent microfocus X-ray source and camera-scintillator system provide sample length measurements facilitating v_P and v_S measurements accurate to better than ± 0.4%. Furthermore, using measured velocities of a polycrystalline quartz sample as a pressure calibrant (uncertainty less than ± 0.30 GPa to 5.82 GPa) it has been demonstrated that experimental pressures can be determined using the compressional wave travel time of the buffer rod with accuracies of ± 0.14 GPa.

VI. ACKNOWLEDGEMENTS

AT acknowledges funding support from a Capital Award for Early Career researchers administrated by UCL on behalf of EPSRC (award number EP/S01800X/1) and internal departmental funding from UCL Earth Sciences which provided the equipment described and used in this study alongside ongoing support provided by the Philip Leverhulme Trust. This work was directly supported by AWE through University Research Agreement No. 30481861. British Crown Owned Copyright 2026/AWE. Published with permission of the Controller of His Britannic Majesty's Stationery Office. We also acknowledge the European

Synchrotron Radiation Facility (ESRF) for provision of synchrotron radiation facilities under proposal ID ES-1524 on beamline ID06-LVP, with related data available at https://doi.org/10.15151/ESRF-ES-2105704088. Finally, we thank E. Samuel for their contribution to the electronic development of the system described in this study.

VII. CONFLICT OF INTEREST STATEMENT

The authors have no conflicts of interest to disclose.

VIII. DATA AVAILABILITY STATEMENT

The derived data supporting the findings of this study are available in the supplementary information. Full supporting data of this study (i.e. unprocessed ultrasonic traces and/or X-ray radiographs) are available from the corresponding author upon reasonable request.

IX. REFERENCES

1. H. B. Huntington, Physical Review **72** (4), 321 (1947).
2. B. S. Li, J. Kung and R. C. Liebermann, Phys Earth Planet In **143**, 559-574 (2004).
3. Z. D. Thomé, W. C. A. Pereira, J. C. Machado, J. M. Seixas and W. Soares, Ieee T Nucl Sci **58** (5), 2452-2458 (2011).
4. R. Williamson and D. Eden, The Journal of the Acoustical Society of America **47** (5B), 1278-1281 (1970).
5. P. M. Nasch, M. Manghnani and R. Secco, Review of scientific instruments **65** (3), 682-688 (1994).
6. N. Yoshimoto, M. Ikeda, M. Yoshizawa and S. Kimura, Physica B: Condensed Matter **219**, 623-625 (1996).
7. J. Carlson and R. Ing, Flow Measurement and Instrumentation **14** (4-5), 193-200 (2003).
8. N. Akashi, J. Kushibiki and F. Dunn, The Journal of the Acoustical Society of America **102** (6), 3774-3778 (1997).
9. J. Kuskibiki, N. Akashi, T. Sannomiya, N. Chubachi and F. Dunn, IEEE transactions on ultrasonics, ferroelectrics, and frequency control **42** (6), 1028-1039 (1995).
10. F. Birch, Elastic Properties and Equations of State **26**, 31-90 (1988).
11. J. A. Connolly, Earth and Planetary Science Letters **236** (1-2), 524-541 (2005).
12. R. Powell, T. Holland and B. Worley, Journal of metamorphic Geology **16** (4), 577-588 (1998).
13. L. Stixrude and C. Lithgow-Bertelloni, Geophysical Journal International **162** (2), 610-632 (2005).
14. G. A. Abers and B. R. Hacker, Geochemistry, Geophysics, Geosystems **17** (2), 616-624 (2016).
15. B. R. Hacker and G. A. Abers, Geochemistry, Geophysics, Geosystems **5** (1) (2004).
16. T. J. Holland, N. F. Hudson, R. Powell and B. Harte, Journal of Petrology **54** (9), 1901-1920 (2013).
17. L. Stixrude and C. Lithgow-Bertelloni, Geophysical Journal International **184** (3), 1180-1213 (2011).
18. L. Stixrude and C. Lithgow-Bertelloni, Geophysical Journal International **237** (3), 1699-1733 (2024).
19. R. K. Cook, The Journal of the Acoustical Society of America **29** (4), 445-449 (1957).
20. N. Cai and D. Wang, Geophysical Research Letters **49** (22), e2022GL100302 (2022).
21. K. L. Darling, G. D. Gwanmesia, J. Kung, B. Li and R. C. Liebermann, Phys Earth Planet In **143**, 19-31 (2004).
22. W. A. Crichton, A. R. Thomson, A. Rosenthal, K. Spektor, D. Druzhbin, B. Winkler, M. Schwarz, P. Wattecamps, J. Kieffer and R. Hino, High Pressure Research **44** (3), 217-247 (2024).
23. R. Farla, S. Bhat, S. Sonntag, A. Chanyshev, S. Ma, T. Ishii, Z. Liu, A. Néri, N. Nishiyama and G. A. Faria, Synchrotron Radiation **29** (2), 409-423 (2022).
24. Y. Higo, Y. Kono, T. Inoue, T. Irifune and K. i. Funakoshi, Synchrotron Radiation **16** (6), 762-768 (2009).
25. Y. Kono, C. Park, C. Kenney-Benson, G. Shen and Y. Wang, Phys Earth Planet In **228**, 269-280 (2014).
26. L. Li, P. Raterron, D. Weidner and J. Chen, Phys Earth Planet In **138** (2), 113-129 (2003).
27. M. Gauthier, D. Lheureux, F. Decremps, M. Fischer, J. P. Itié, G. Syfosse and A. Polian, Review of scientific instruments **74** (8), 3712-3716 (2003).
28. Y. L. Godec, M. T. Dove, S. A. Redfern, M. G. Tucker, W. G. Marshall, G. Syfosse and J.-M. Besson, International Journal of High Pressure Research **21** (5), 263-280 (2001).
29. T. Yu, C. Prescher, Y. J. Ryu, F. Shi, E. Greenberg, V. Prakapenka, P. Eng, J. Stubbs, Y. Kono and G. Shen, Minerals **9** (11), 715 (2019).
30. J. Besson, S. Klotz, G. Hamel, I. Makarenko, R. Nelmes, J. Loveday, R. Wilson and W. Marshall, International Journal of High Pressure Research **14** (1-3), 1-6 (1995).
31. L. Khvostantsev, V. Slesarev and V. Brazhkin, High Pressure Research **24** (3), 371-383 (2004).
32. Y. Zhao, R. B. V. Dreele and J. G. Morgan, International Journal of High Pressure Research **16** (3), 161-177 (1999).
33. R. Hrubiak and B. T. Sturtevant, High Pressure Research **43** (1), 23-39 (2023).
34. J. L. Jordan, R. L. Rowland, J. Greenhall, E. K. Moss, R. C. Huber, E. C. Willis, R. Hrubiak, C. Kenney-Benson, B. Bartram and B. T. Sturtevant, Polymer **212**, 123164 (2021).

35. E. P. Papadakis, the Journal of the Acoustical Society of America **45** (6), 1547-1555 (1969).
36. M. Noda, T. Inoue, T. Tsuchiya and Y. Higo, High Pressure Research **42** (3), 278-293 (2022).
37. Y. D. Sinelnikov, G. Chen and R. C. Liebermann, High Pressure Research **24** (1), 183-191 (2004).
38. W. Song, Q. Tang, C. Su, X. Chen and Y. Liu, High Pressure Research **41** (1), 75-87 (2021).
39. X. Wang, T. Chen, X. Qi, Y. Zou, J. Kung, T. Yu, Y. Wang, R. C. Liebermann and B. Li, Journal of Applied Physics **118** (6) (2015).
40. J. Wang, Z. Mao, F. Jiang and T. S. Duffy, Physics and Chemistry of Minerals **42** (3), 203-212 (2015).
41. R. J. Angel, M. Bujak, J. Zhao, G. D. Gatta and S. D. Jacobsen, Applied Crystallography **40** (1), 26-32 (2007).
42. H. Mao, J.-A. Xu and P. Bell, Journal of Geophysical Research: Solid Earth **91** (B5), 4673-4676 (1986).
43. G. Mingardi, J. Gasc, M. Ardit, R. J. Angel, W. A. Crichton, D. Druzhbin, J. Aubry, A. Schubnel and M. Alvaro, Contributions to Mineralogy and Petrology **180** (3), 21 (2025).
44. F. Birch, Geophysical Journal International **4** (Supplement_1), 295-311 (1961).
45. A. Néri, L. Man, J. Chantel, R. Farla, G. Bauer, S. Linhardt, T. Boffa Ballaran and D. J. Frost, Review of Scientific Instruments **95** (1) (2024).

X. SUPPLEMENTARY FIGURES

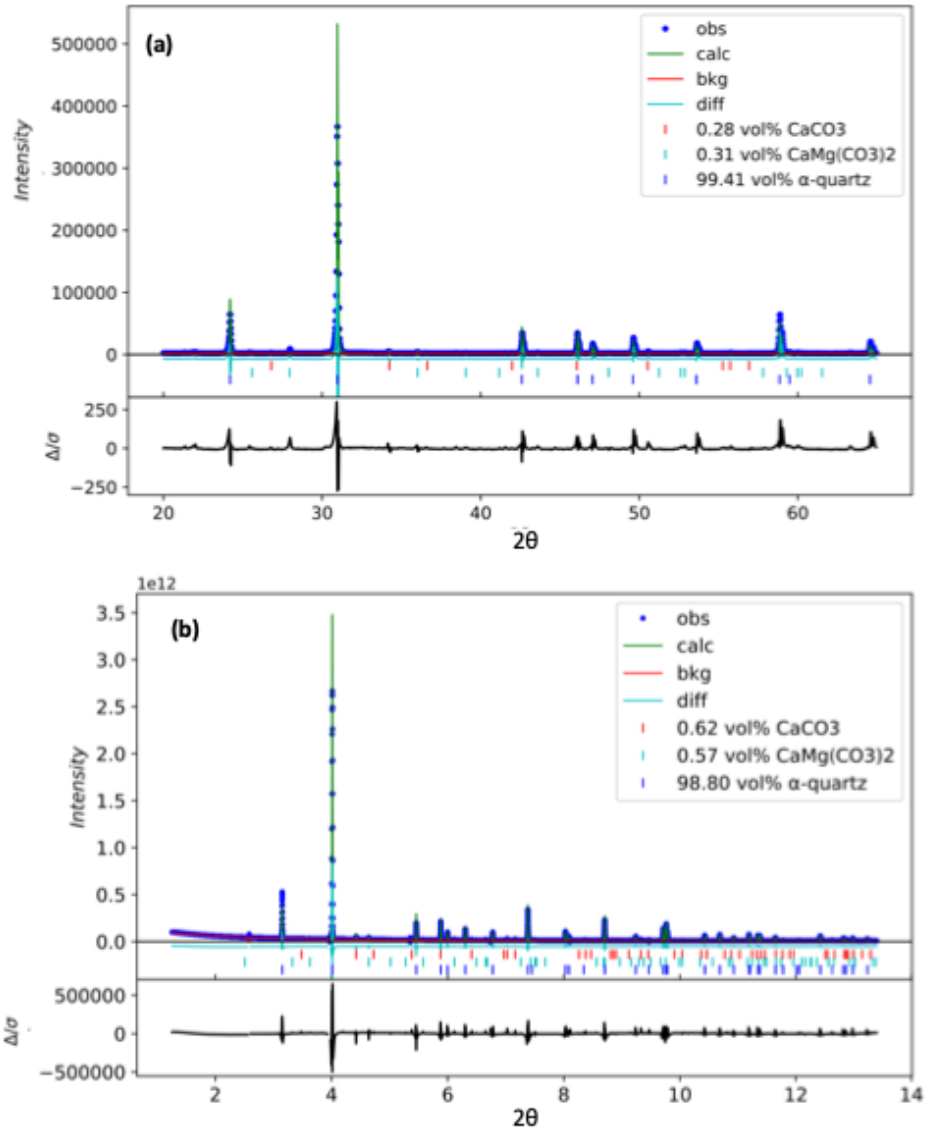

Supplementary Figure 1: *Rietveld refinement of powder X-ray diffraction pattern of the novaculite starting material collected using* ***(a)*** *Fe-filtered Co Kα radiation and* ***(b)*** *monochromatic synchrotron X-rays at ID06-LVP.*

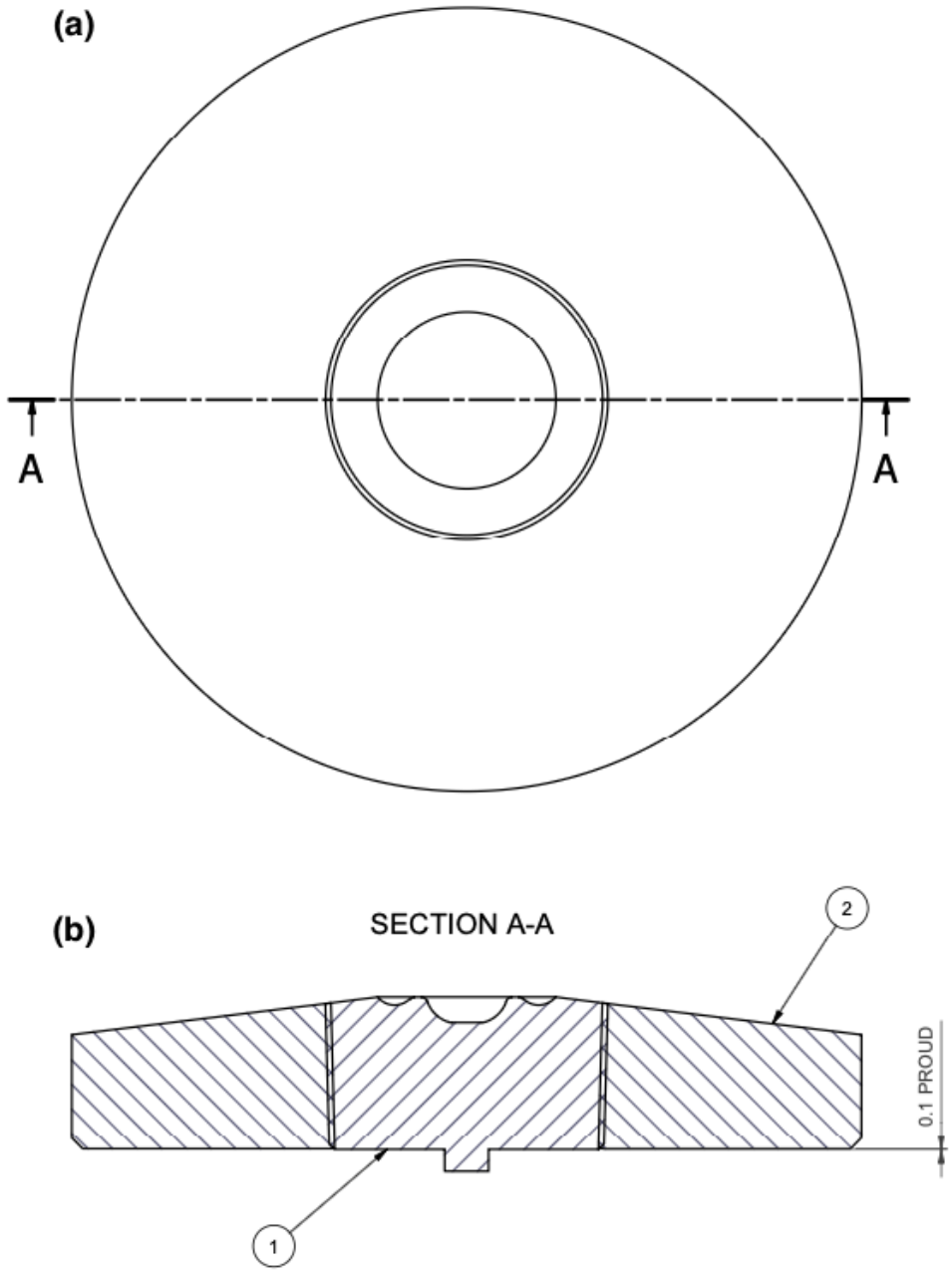

Supplementary Figure 2: *Design drawing of the toroidal anvils used in the present study in* ***(a)*** *plan and* ***(b)*** *profile view.*

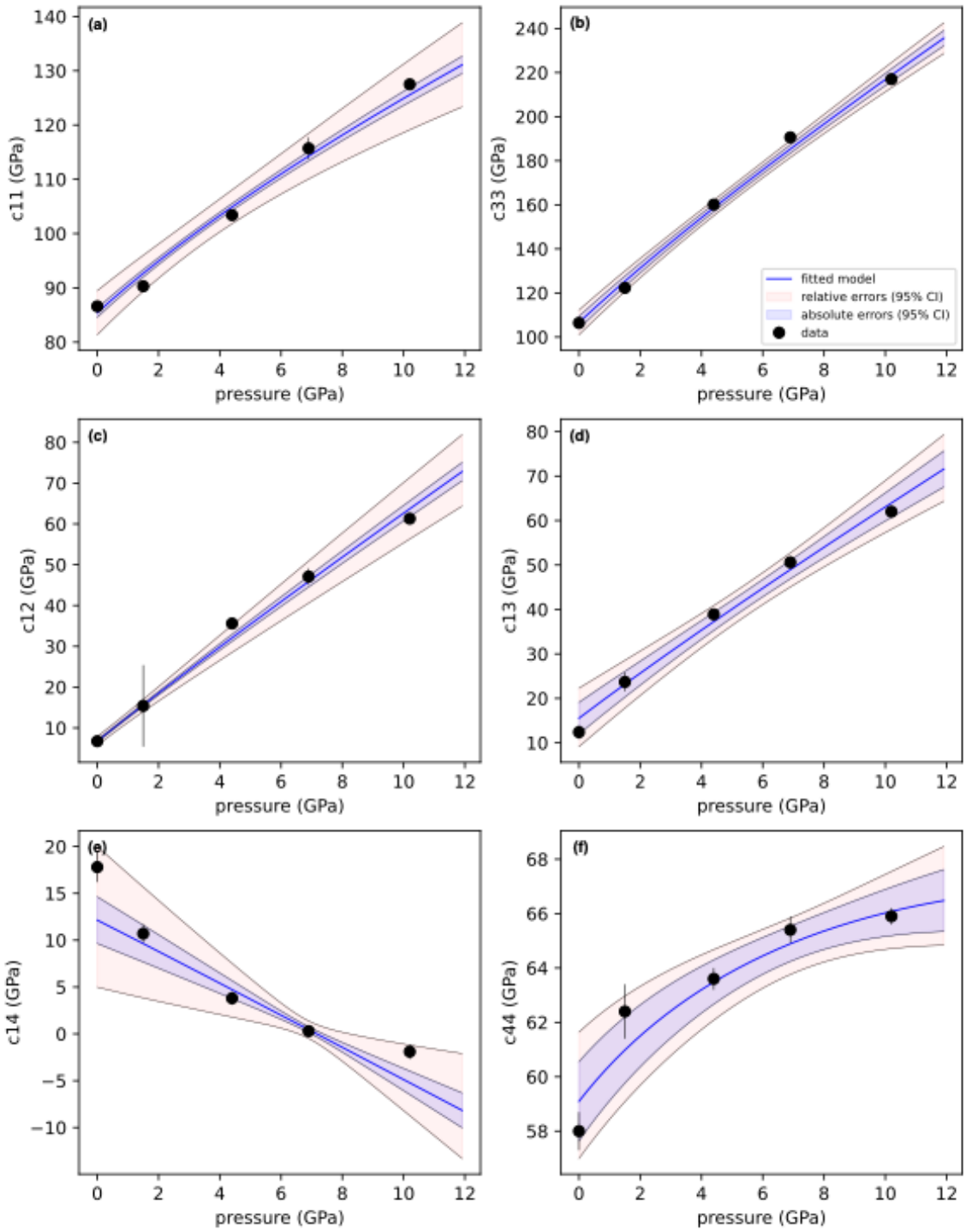

Supplementary Figure 3: *Refitted elasticity data for the elastic constants of quartz from Wang et al. (2015) using equations 3-5. Black symbols and error bars show reported data and uncertainties. Blue confidence intervals show the 2-sigma uncertainty in the fitted regressions assuming absolute uncertainty scaling – note many more than 4.55% of data fall outside these confidence intervals. Red confidence intervals show the 2-sigma uncertainty in fitted regression assuming reported uncertainties only provide relative scaling.*

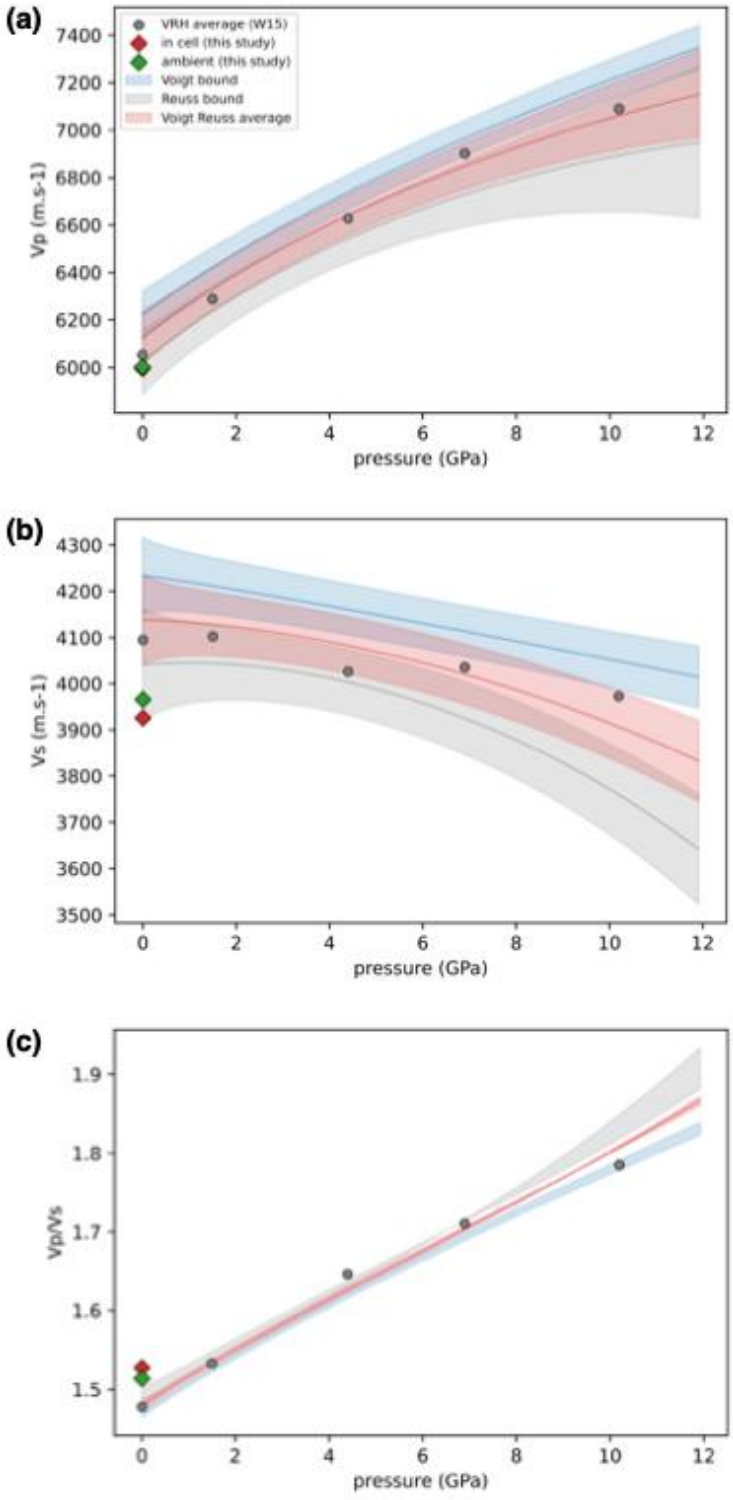

Supplementary Figure 4: *Modelled values for the Voigt (blue), Reuss (grey) and Voigt-Reuss-Hill average (VRH, red)* ***(a)*** v_P, ***(b)*** v_S *and* ***(c)*** v_P/v_S *with pressure. 95% confidence intervals are shown as coloured bands. Grey data with uncertainties are the literature reported values (plus 2-sigma uncertainties) of VRH velocities for quartz (Wang et al., 2015). Green and red diamonds are the starting material and sample velocities respectively, measured at ambient conditions and 100 bar (assumed effectively 0 GPa) in this study.*

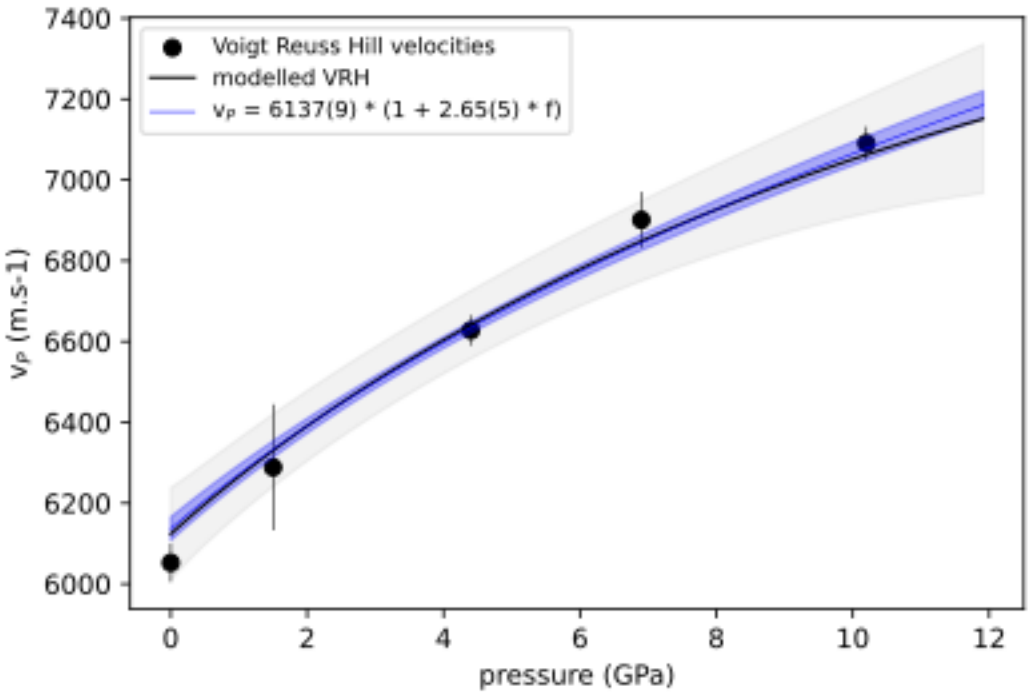

Supplementary Figure 5: *Modelled v_P^{VRH} vs pressure for quartz with 2-sigma uncertainty from eq 6 (blue) compared to literature data (black) and fits based on eq 3-5 (black curve and grey confidence limits).*

Supplementary Table 1: *Sample lengths, travel time measurements, derived velocities and pressure conditions as a function of oil pressure. All calculated properties are derived as described in the text and all uncertainties (which are fully propagated from all measurement and fitting uncertainties) are reported at the 1σ level.*